Front. Energy 2021, 15(3): 700–709
https://doi.org/10.1007/s11708-021-0735-2

RESEARCH ARTICLE

Junying LIU, Zhidong WEI, Wenfeng SHANGGUAN

Enhanced photocatalytic water splitting with surface defective $SrTiO_3$ nanocrystals

Abstract Surface reconstructed $SrTiO_3$ nanocrystals were synthesized by a thermal treatment process in presence of $NaBH_4$ and $SrTiO_3$ nanocrystals. The surface reconstruction of $SrTiO_3$ nanocrystals is attributed to the introduction of surface oxygen vacancies or Ti sites (such as Ti^{3+} and Ti^{2+}) during the hydrogenation treatment process. The light absorption and the charge transfer ability of $SrTiO_3$ nanocrystals are simultaneously enhanced due to surface oxygen vacancies or Ti sites (such as Ti^{3+} and Ti^{2+}), which are beneficial to photocatalytic water splitting. Meanwhile, these defects also change the redox potential of the photocatalysts. Since there existed a synergistic effect between the three, the ratio of hydrogen to oxygen production was also regulated.

Keywords $SrTiO_3$, surface reconstruction, oxygen vacancies, photocatalytic water splitting*

1 Introduction

Photocatalysis, as an energy-efficient route to solve the problem of a non-renewable energy shortage, has received widespread attention [1–8]. Up to now, varieties of semiconductor materials have been employed in photocatalytic H_2 production, such as TiO_2, $SrTiO_3$, CdS, g-C_3N_4, etc. [9–13], among which, perovskite structural semiconductor $SrTiO_3$ has been considered as a promising photocatalyst for water splitting due to its suitable conduction band structure, and dramatic physical and chemical properties [14]. However, the photocatalytic efficiency of $SrTiO_3$ is limited by the quick recombination of photogenerated carriers [15–17]. Thus, it is of great significance to enhance the separation of photogenerated charges of photocatalysts for improving the photocatalytic activity. To this end, a variety of strategies have been made to promote charge separation, such as forming heterojunctions [18–21], loading cocatalyst [10,22,23], and controlling crystal facets [24–26], etc.

Recently, some studies have found that highly active photocatalysts are obtained by regulating the surface structure of photocatalysts by introducing oxygen vacancies into the near-surface region [27–31]. For example, Chen et al. [32] prepared TiO_2 with a disordered surface by using the high-temperature hydrogenation method and found that disordered surface-induced mid-gap electronic state upshifted the edge of the valence band of TiO_2, thus preventing rapid charge recombination. Wang et al. [33] reported that substoichiometric WO_{3-x} was prepared by hydrogen treatment and found that photostability and photoactivity of WO_3 for water oxidation were simultaneously enhanced due to the introduction of oxygen vacancies. The above studies demonstrate that the introduction of oxygen vacancies to regulate the surface atomic arrangement and electronic structure can enhance the charge transfer ability of the interface between photocatalyst and electrolyte, so as to improve the photocatalytic performance. In addition, it has been proved that the high concentration of Ti^{3+} sites is in favor of the adsorption of water molecules, and oxygen vacancies with Ti^{3+} facilitate the dissociation of water [34,35]. However, few studies focus on the effect of oxygen vacancies on the overall water splitting of the photocatalyst. Thus, it is of great significance to study the influence of oxygen vacancies on photocatalytic overall water splitting.

Received Nov. 19, 2020; accepted Dec. 20, 2020; online Apr. 8, 2021

Junying LIU (✉)
Institute of Physical Chemistry, University of Hamburg, Grindelallee 117, 20146 Hamburg, Germany
E-mail: junying.liu@chemie.uni-hamburg.de

Zhidong WEI, Wenfeng SHANGGUAN (✉)
Research Center for Combustion and Environment Technology, Shanghai Jiao Tong University, Shanghai 200240, China
E-mail: shangguan@sjtu.edu.cn

Special Issue—Photocatalysis: From Solar Light to Hydrogen Energy (Guest Editors: Wenfeng SHANGGUAN, Akihiko KUDO, Zhi JIANG, Yuichi YAMAGUCHI)

In this work, $SrTiO_3$ nanocrystals were synthesized by using a molten salts method and the surface of $SrTiO_3$ nanocrystals was reconstructed with a thermal treatment process in presence of $NaBH_4$. After surface reconstruction, a disordered layer of about 1.6 nm in thickness was formed on the surface of the $SrTiO_3$ nanocrystals due to the introduction of oxygen vacancies, leading to an improved photocatalytic performance of all $SrTiO_3$ samples (STO-*T*), which was caused by the enhanced light absorption, charge transferability, and the reduction ability. Besides, the introduction of oxygen vacancies affects the ratio of H_2 and O_2 of overall water splitting.

2 Experimental

2.1 Chemicals and reagents

The $SrCO_3$, NaCl, KCl, and chloroplatinic acid (H_2PtCl_6) were purchased from Sinopharm Chemical Reagent Co., Ltd. The TiO_2 (P25) was offered by Nippon Aerosil. All the reagents were analytical grade. The water was deionized water with a resistivity of 18.2 MW·cm.

2.2 Preparation of $SrTiO_3$ nanocrystals

Typically, 1.476 g $SrCO_3$ and 0.79 g TiO_2 were mixed and ground with 22 g of NaCl and KCl mixed powder (with a molar ratio of 50:50) in an agate mortar, and then transferred to a crucible which was heated at a ramping rate of 5°C/min to 850°C in a muffle furnace for 6 h. Then, natural cooling to room temperature, the products were washed with hot water several times. The products were collected by centrifugation, following the drying at 80°C overnight. Finally, the products were obtained.

2.3 Preparation of surface reconstructed $SrTiO_3$ nanocrystals

Typically, 1.0 g $SrTiO_3$ was mixed and ground with 0.25 g $NaBH_4$ for 20 min in a mortar. Then, the mixture was heated at a ramping rate of 5°C/min to 320°C–380°C for 60 min at N_2 atmosphere in a tubular furnace. Then, the products were washed with hot water and ethanol several times and dried at 80°C. The resulting products were named STO-*T*, where *T* is the reaction temperature (*T* = 320°C, 350°C, and 380°C).

2.4 Characterization

The crystal structures of the as-prepared samples were determined using a powder X-ray diffractometer (XRD) with Cu Kα radiation source (D8 Advance, Bruker). A field-emission scanning electron microscopy (FE-SEM, Hitachi S4800) and transmission electron microscopy (TEM, Talos F200X, FEI) were used to investigate the morphologies of the samples. Raman spectra were obtained on a Senterra R200-L Raman microscope (Bruker Optics, Germany). The valency of the constituent elements was determined using X-ray photoelectron spectroscopy (XPS, Axis-Ultra, Shimadzu). The UV-visible (UV-Vis) diffuse reflectance spectra were measured on a Shimadzu UV-2450 spectrophotometer. The photoluminescence (PL) spectra were determined using a PerkinElmer LS 55 spectrophotometer at room temperature. The XPS was measured by using an AXIS UltraDLD (Kratos Group, Shimadzu) spectrometer at 300 W with Mg Kα X-rays source. The thermogravimetric analysis (TGA) was measured by an STA 449 F3 Jupiter (Netzsch Instruments, Germany). The electron paramagnetic resonance (EPR) spectrum was recorded by EMX-8 (Bruker BioSpin Corp., Germany).

2.5 Photocatalytic water splitting

The photocatalytic H_2 production tests and overall water splitting reaction were carried out in a closed gas circulation system with a Pyrex reaction cell. The samples (0.1 g) were dispersed in 100 mL aqueous methanol (with a volume percentage of 20 vol.%, as sacrificial reagents) solution and distilled water without any sacrificial agent by sonication and stirring in the Pyrex reaction cell, respectively. After evacuated by the vacuum pump, the reactor was irradiated with a 300 W Xe lamp with the photocatalytic reaction temperature maintained at 20°C–25°C by a water bath. The H_2 and O_2 production were determined by an online Hua'ai GC9160 gas chromatography (MS-5A, TCD detector, Ar as carrier gas). For photocatalytic hydrogen evolution and overall water splitting reaction, Pt (with a volume percentage of 1.0 wt.%) as co-catalyst was *in situ* photo-deposited on the samples with $H_2PtCl_6 \cdot 6H_2O$ as Pt precursor.

2.6 Photoelectrochemical measurements

A conventional three-electrode system was used to examine the photoelectrochemical properties of the samples on a PARSTAT 4000 electrochemical workstation. An fluorine doped TinOxide (FTO) photoanode with STO samples, Ag/AgCl, and platinum foil were used as the working electrode (1.0 cm×1.0 cm), the reference electrode, and the counter electrode, respectively. Na_2SO_4 (0.1 mol/L) was used as the electrolyte solution. For photocurrent measurements, a 500 W Xe lamp coupled with an AM 1.5 filter was used as the light source, with the light intensity set at 100 mW/cm^2. The electrochemical impedance spectroscopy (EIS) spectra were recorded under a sinusoidal AC perturbation signal of 10 mV over the frequency range from 100 kHz to 0.1 Hz. The Mott-Schottky plots were obtained with a scan rate of 5 mV/s^1 at the frequency of 1000 Hz. The linear sweep voltammetry (LSV) was obtained in the range of −1.4–0.0 V with a scanning rate of 10 mVs^{-1}

3 Results and discussion

The crystal structures of the STO samples were characterized by XRD. As shown in Fig. 1, all the STO samples display several diffraction peaks located at 2θ of 22.7°, 32.3°, 39.9°, 46.4°, 52.3°, 57.7°, 67.8°, and 77.1°, corresponding to (100), (110), (111), (200), (210), (211), (220), and (310) crystal planes of cubic $SrTiO_3$ (PDF 79-0174) [26]. Besides, the XRD patterns of the STO-*T* samples were similar to the original cubic phase $SrTiO_3$, indicating that no structural changes occurred and impurity phases appeared in STO after $NaBH_4$ treatment, which was in good agreement with the SEM results. However, it is worth noting that the intensity of the (110) peak decreases, resulting from the disordered surface of the (110) crystal planes after $NaBH_4$ treatment, which can also be observed in TEM.

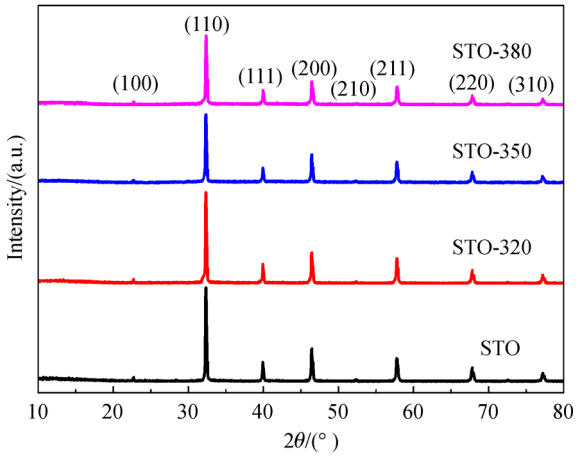

Fig. 1 XRD patterns of STO, STO-320, STO-350, and STO-380.

The morphology of pristine $SrTiO_3$ and STO-350 was investigated by using SEM. As demonstrated in Figs. 2(a) and 2(b), pristine $SrTiO_3$ shows a nano cubic shape with truncated edges. The particle size is about 200 nm. After thermal hydrogenation, STO-350 still retained the original morphology of pristine $SrTiO_3$ (cube shape with truncated edges). TEM was used to further observe the morphologies of the STO samples, as displayed in Figs. 2(c) and 2(d), and Fig. S1 in Electronic Supplementary Material (ESM). It can be seen that the particle size and morphology of STO and STO-350 do not change after hydrogenation treatment. Both STO and STO-350 exhibit cube shapes with average sizes of approximately 200 nm, which is consistent with SEM results. Moreover, before hydrogenation treatment, the crystal lattice fringes of pristine $SrTiO_3$ nanocrystals are clear and the crystal lattice plane spacing is 0.27 nm, corresponding to the (110) crystal plane of cubic $SrTiO_3$ (Fig. 2(c)) [27]. However, after hydrogenation treatment, the lattice fringes of STO-350 become a little blurry and a disordered layer with a thickness of 1.6 nm appears (Fig. 2(d)), which indicates that the surface of STO-350 is

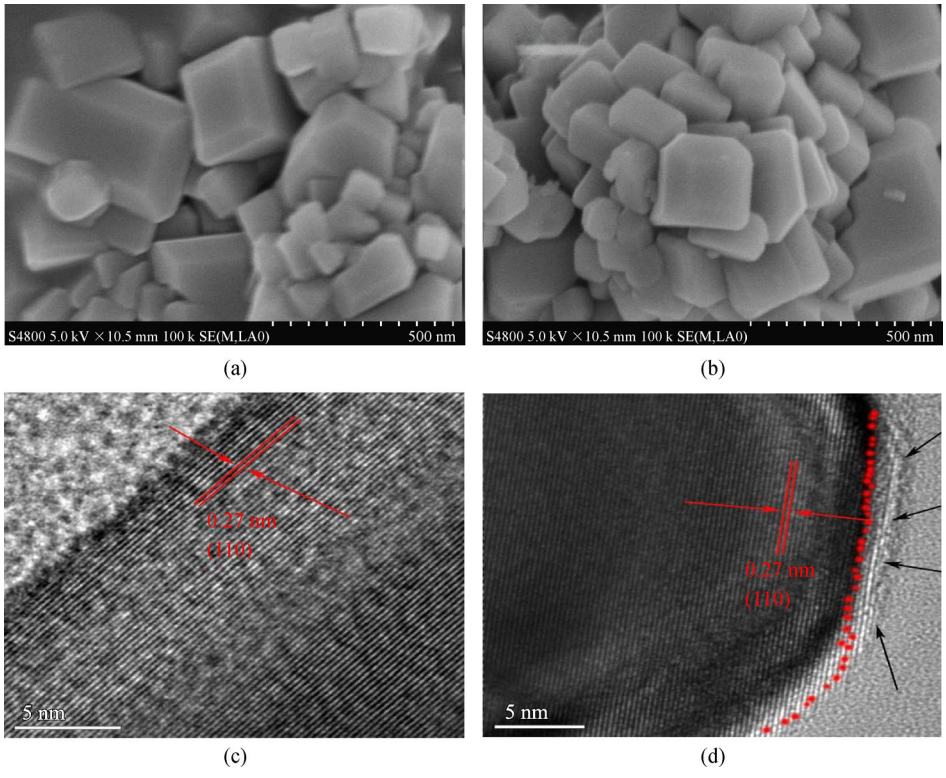

Fig. 2 SEM and HRTEM images.
(a) SEM image of pristine $SrTiO_3$; (b) SEM image of STO-350; (c) HRTEM image of pristine $SrTiO_3$; (d) HRTEM image of STO-350.

reconstructed. As presented in Fig. 3 and Fig. S2, a high-angle annular dark-field scanning TEM (HAADF-STEM) was employed to resolve the elemental composition spatially. Sr, Ti, and O are observed from the mapping images. Moreover, Sr, Ti, and O are colocalized in a square with truncated corners, which is attributed to the cubic shape with truncated edges observed in the HAADF image.

The Raman spectra of pristine $SrTiO_3$ and STO-350 is illustrated in Fig. 4. It can be observed that both $SrTiO_3$ and STO-350 show two broad bands in the regions of 250–400 cm^{-1} and 600–800 cm^{-1}, which are in accord with the results in Ref. [36]. Meanwhile, both pristine $SrTiO_3$ and STO-350 display several peaks at 190, 250–348, 539, 624–719, and 795.5 cm^{-1}, corresponding to different modes of TO_2 (O-Sr-O), TO_3 (O-Sr-O), TO_4 (O-Sr-O), LO (Ti-O-Ti), and LO_4 (Ti-O), respectively [37]. This demonstrated that the hydrogenation treatment did not change the crystal structure of pristine $SrTiO_3$. However, due to the disordered layer formed on the surface of STO-350, the intensity of the Raman spectra of STO-350 is significantly lower than that of pristine $SrTiO_3$ after hydrogenation treatment.

To explore the effect of hydrogenation treatment on the surface structure, the surface chemical states of STO and STO-350 were investigated by using XPS. The Sr 3d, Ti 2p, and O 1s XPS spectra of STO and STO-350 are depicted in Fig. 5. The Ti 2p spectrum of pristine STO can be fitted into two peaks at 458.3 and 464.1, respectively, corresponding to the Ti 2p3/2 and Ti 2p1/2 binding states. Nevertheless, after the hydrogenation treatment, the peak corresponding to Ti 2p1/2 bonding can be divided into three peaks at 456.1, 456.8, and 458.5 eV, assigning to the chemical states of Ti^{2+}, Ti^{3+}, and Ti^{4+}, respectively [38]. In addition, compared to the spectra of STO, the peaks of Sr 3d, Ti 2p, and O 1s of STO-350 moves 0.2 eV toward higher binding energy. This may be caused by defects such as oxygen vacancies and/or Ti^{3+} (or/and Ti^{2+}) [27,29,39]. Moreover, the defects induced by the hydrogenation treatment increase the equilibrium electron density, which also pushes the Fermi level upward. Figure 5(c) shows the O 1s XPS spectra of STO and STO-350. For the

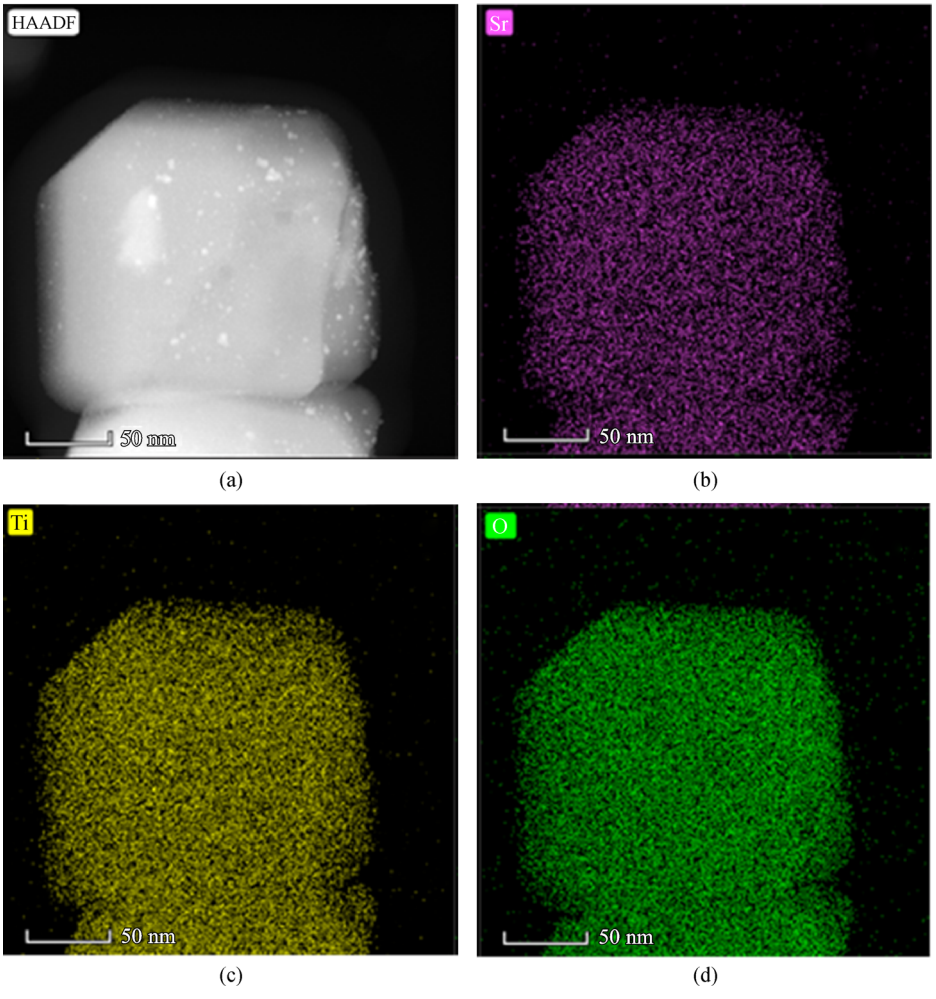

Fig. 3 Elemental mapping of STO-350 sample by HAADF-STEM.
(a) HAADF image; (b) Sr; (c) Ti; (d) O.

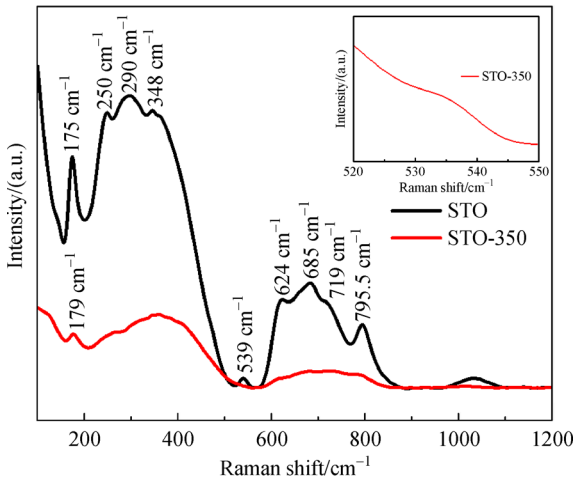

Fig. 4 Raman spectra of pristine $SrTiO_3$ and STO-350.

STO sample, it could be fitted to three peaks at 528.6 eV, 529.4 eV, and 531.7 eV, which correspond to the lattice oxygen ion, oxygen vacancy, and adsorption oxygen in STO, respectively [37]. After hydrogenation treatment, the intensity of the oxygen vacancy peak in STO-350 becomes stronger than that in pristine STO, indicating that the surface oxygen vacancy concentration in STO-350 increases. Figure 5(d) is the electron paramagnetic resonance (EPR) spectrum of STO and STO-*T* samples. Pristine STO displays a lower EPR signal, but the STO-*T* samples show stronger EPR signals at $g = 2.002$, which is caused by the combination of oxygen vacancy with an electron [40]. Meanwhile, the intensity of the EPR signal increases along with the treatment temperature, representing the concentration of oxygen vacancy in the STO-*T* samples raises.

To investigate and determine the concentration of oxygen vacancies introduced into STO-*T*, TGA was performed in a flowing air/nitrogen mixture gas. The increased mass of the samples is attributed to the refilling of oxygen vacancy in the samples. As shown in Fig. 6, the weight of all hydrogenated $SrTiO_3$ samples increases along with the temperature. This weight gain is resulted from the refilling of the oxygen vacancy, simultaneously depending on the oxygen vacancy concentration introduced by hydrogenation treatment. After air/nitrogen mixed gas treatment, relative to pristine $SrTiO_3$, the mass percentages of STO-320, STO-350, and STO-380 are 101.35%, 102.26%, and 102.71%, respectively. Through these

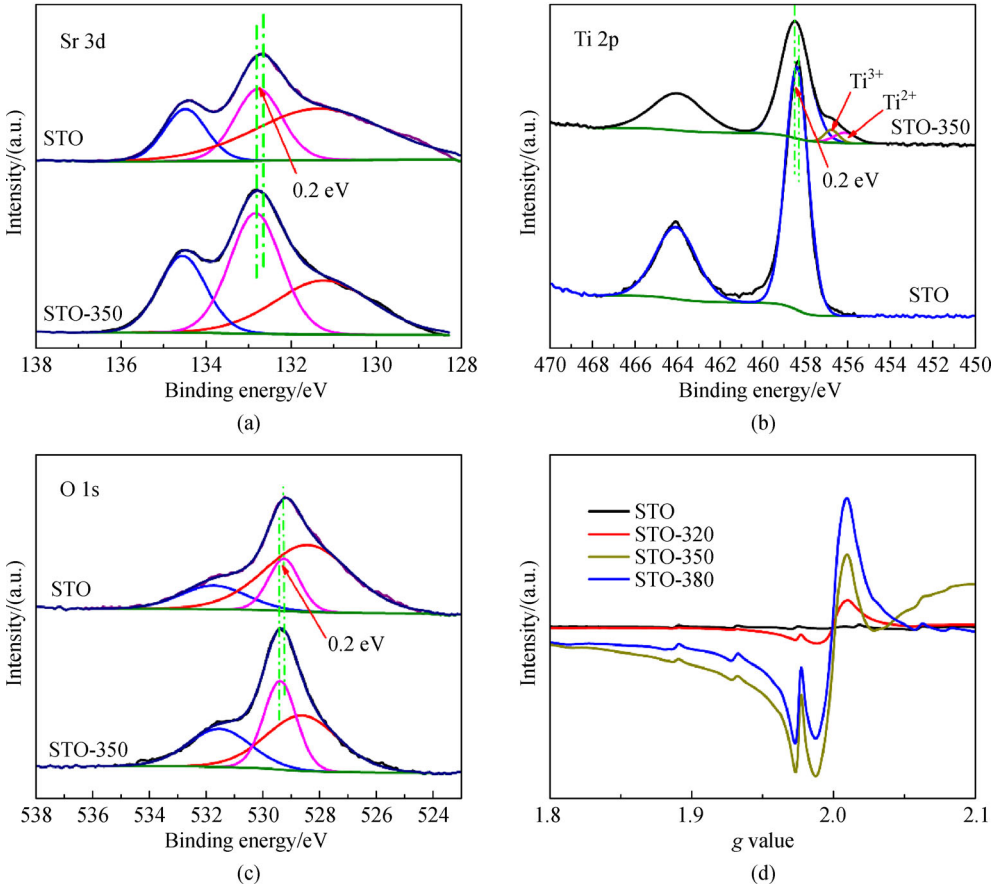

Fig. 5 (a) Sr 3d XPS spectra; (b) Ti 2p XPS spectra; (c) O 1s XPS spectra; (d) EPR spectra of pristine $SrTiO_3$ and STO-350.

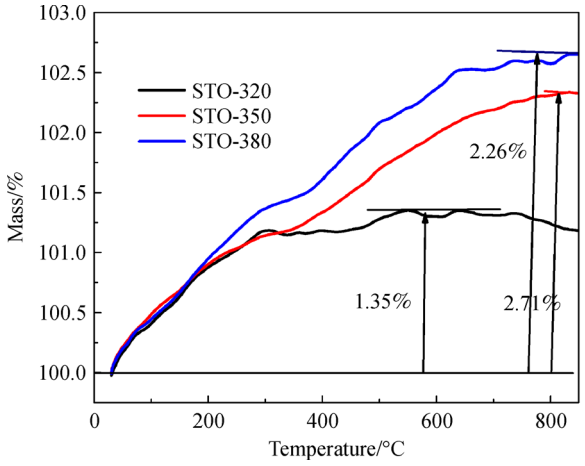

Fig. 6 TGA curve of STO-320, STO-350, and STO-380.

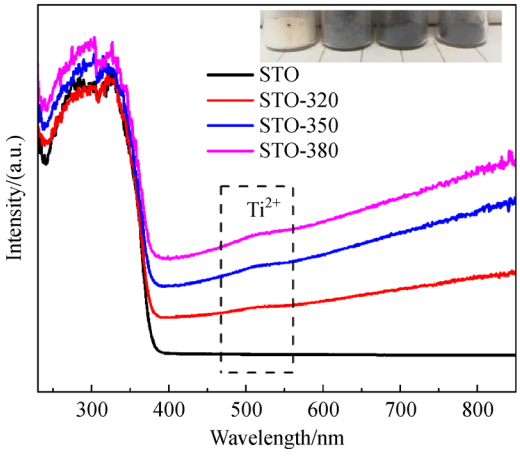

Fig. 7 UV-vis diffuse reflectance spectra of STO samples (The insets are photographs of pristine $SrTiO_3$ and STO-*T* samples).

mass percentages, the calculated oxygen vacancy concentration in the STO-*T* samples are 5.58%, 9.85%, and 11.7%, respectively. In addition, when the temperature is higher than 800°C, the STO-320 shows a weight-loss stage in the TGA curves, which can be attributed to the loss of chemically absorbed water and the escape of oxygen atoms from the surface of $SrTiO_3$ at a high temperature [24].

The UV-vis diffuse reflection spectra of STO, STO-320, STO-350, and STO-380 are presented in Fig. 7. The light absorption of STO-*T* samples is higher than that of pristine $SrTiO_3$. Compared to pristine $SrTiO_3$, the STO-*T* samples display a broad absorption band from 400 nm to the infrared region, which is caused by oxygen vacancy and Ti^{3+} on the $SrTiO_3$ surface. The light absorption enhances along with the reaction temperature, which is consistent with the color change of the STO-*T* samples (the inset in Fig. 7). The color of the STO samples gradually changes from white to dark gray. Besides, a relatively small absorption packet appears at 450–550 nm, corresponding to the absorption induced by Ti^{2+} [41].

The flat band potential and valence band of pristine $SrTiO_3$ and STO-350 were obtained by Mott-Schottky plots and XPS valence band spectra. As shown in Fig. 8(a), the flat band potentials of pristine $SrTiO_3$ and STO-350 are −1.28 eV and −1.42 eV (vs. Ag/AgCl), respectively. Generally, the flat-band potential is 0.1–0.2 eV higher than the conduction band potential, so the flat band potential values of pristine $SrTiO_3$ and STO-350 are modified to −1.283 eV and −1.423 eV (vs. normal hydrogen electrode (NHE)). The flat band potential of STO-350 is higher than that of pristine $SrTiO_3$, which is attributed to the oxygen vacancy induced by hydrogenation treatment. Here oxygen vacancies increase the donor density in $SrTiO_3$, improving the charge transfer ability of $SrTiO_3$. In addition, the increasing donor density makes the Fermi level move up. The XPS valence band for pristine $SrTiO_3$ and STO-350 are shown in Fig. 8(b). It is observed that the valence bands of pristine $SrTiO_3$ and STO-350 are 1.98 eV and 1.83 eV (vs. vacuum, 1.84 eV, and 1.69 eV, vs. NHE). Due to the introduction of oxygen vacancy, the valence band of STO-

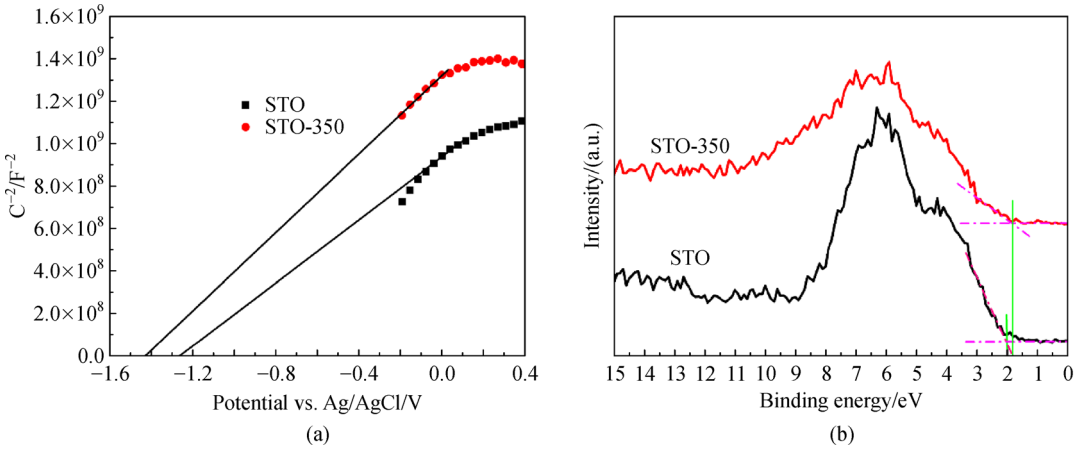

Fig. 8 Flat band potentials of pristine $SrTiO_3$ and STO-350.
(a) Mott-Schottky plot of pristine $SrTiO_3$ and STO-350; (b) XPS valence band spectra of pristine $SrTiO_3$ and STO-350.

350 shifts toward lower energy.

The PL spectra was used to investigate the effect of surface oxygen vacancy on the charge separation of STO-*T* samples. Figure 9 shows PL spectra of STO, STO-320, STO-350, and STO-380. It is observed that the PL intensity of STO-*T* samples is related to the hydrogenation treatment temperature. The higher treatment temperature corresponds to the lower PL intensity of the STO-*T* samples, which indicates that the charge separation ability of photogenerated carriers increases with the processing temperature raising. Besides, based on the results of TGA, the higher treatment temperature corresponds to the higher oxygen vacancy concentration. In other words, the increase of oxygen vacancy concentration on the STO-*T* surface could promote the separation of photogenerated charges in STO-*T* samples. For the STO-380 sample, the PL intensity increases to the highest, which is due to the fact that the excessive oxygen vacancies allow electron-hole pairs to recombine on the surface.

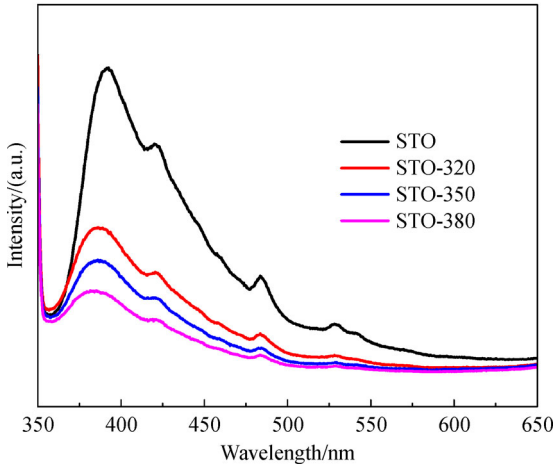

Fig. 9 PL spectra of pristine $SrTiO_3$, STO-320, STO-350, and STO-380.

To further verify the effect of surface oxygen vacancy on the charge separation of STO-*T* samples, the transient photocurrent response of $SrTiO_3$ and STO-350 was performed. As shown in Fig. 10(a), STO-350 with oxygen vacancies shows significantly enhanced photocurrent in comparison with the pristine $SrTiO_3$, which indicates that surface oxygen vacancies effectively promote the photo-induced charge separation of STO-*T* samples. The current density of STO-350 is about two times higher than that of pristine $SrTiO_3$, which is consistent with the enhanced photocatalytic activity. EIS is a powerful tool to study the interface charge transfer process. As shown in Fig. 10(b), the semicircular diameter of STO-350 was smaller than that of STO, and the small semicircular diameter indicates a smaller interface charge transfer resistance, which further demonstrates that surface oxygen vacancy could efficiently promote the charge transfer. It is well known that oxygen vacancies can serve as electron donors and increase donor density. With the increase of donor density, the charge transport in $SrTiO_3$ can be improved. Besides, the Fermi level of $SrTiO_3$ also moves up with the increasing donor density. This change in the Fermi level also improves the charge separation ability at the STO/electrolyte interface.

The photocatalytic overall water splitting experiment of STO samples was performed in pure water under UV-visible light irradiation, and Pt was photo-loaded *in situ* on samples to boost H_2 and O_2 generation in advance. As shown in Fig. 11, the H_2 evolution rate is increasing with the increasing oxygen vacancies, but when overdose, it will decrease. Moreover, the ratios of H_2 and O_2 evolution rate are about 1.76, 1.82, 2.07, and 1.91, respectively, which is caused by the introduction of oxygen vacancies that changes the redox potential of the photocatalyst. To further investigate the oxygen vacancies on the reduction ability of the samples, the photocatalytic hydrogen production tests with sacrificial reagents were also conducted. Figure S3(a) shows the time-dependent photo-catalytic hydrogen production of STO, STO-320, STO-

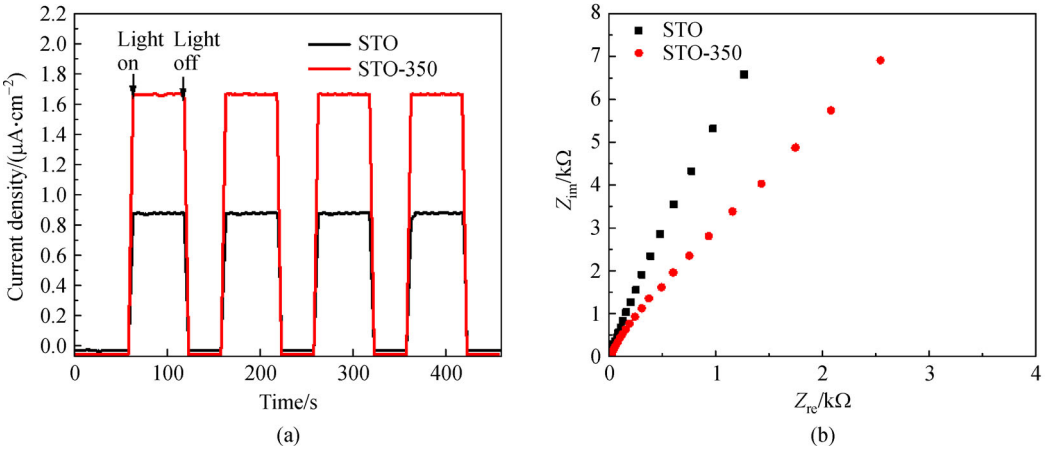

Fig. 10 Photoelectric properties.
(a) Transient photocurrent response; (b) EIS plots of STO and STO-350 (Z_{im}: imaginary resistance, Z_{re}: real resistance).

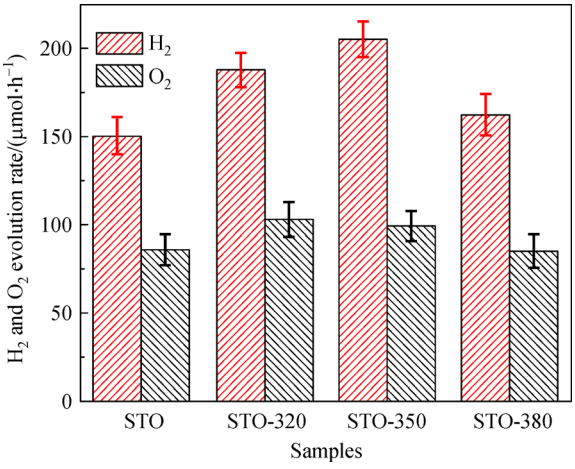

Fig. 11 Specific H_2 and O_2 evolution activities of STO samples.

350, and STO-380. It is observed that all the STO-*T* samples show a higher activity than pristine STO. The average hydrogen production rate of pristine STO is 130.4 μmol/h. With the increasing treatment temperature, the hydrogen production activity increases. The hydrogen production rate of STO-350 reaches a maximum of 202.8 μmol/h, which is about 1.5 times that of pristine STO. The increase of photocatalytic activity is attributed to oxygen vacancies, which acts as electron donors to enhance the donor density in semiconductor photocatalyst and simultaneously improve the charge transfer ability of photocatalyst. Besides, the increasing donor density makes the Fermi level upper shifts, synchronously increasing the degree of band bending and facilitating charge separation at the photocatalyst/electrolyte interface. However, too higher a temperature results in an excess amount of oxygen vacancy concentration, which is bad for photocatalytic reaction. The photocatalytic activity of STO-380 decrease, and the rate of hydrogen production drops to 182.1 μmol/h. This may result from the excessive oxygen vacancies formed on the $SrTiO_3$ surface act as the charge recombination centers and thus decreases the catalytic activity. The stability test of STO-350 is carried out as shown in Fig. S3(b). It is found that the STO-350 sample still maintains a stable photocatalytic activity after three recycles, which demonstrates that STO-350 has a good stability.

Due to the effect of the over-potential of the water-splitting reaction on the photocatalytic H_2 evolution rate, the polarization curves of the photocatalysts for the hydrogen evolution reaction were measured [42]. The LSV curves of pristine $SrTiO_3$ and STO-350 are shown in Fig. 12(a). STO-350 possesses a higher cathodic current density at the same potential than pristine $SrTiO_3$. STO-350 shows a slight anodic shift of ca. 0.1 V in the onset-potential for the hydrogen evolution reaction, which indicates that STO-350 has a lower over-potential, revealing that the H_2 production ability is also prompted. Moreover, cyclic voltammetry (CV) was employed to explore the photoelectrochemical properties of the photocatalysts. As shown in Fig. S4, STO-350 has a higher current density, further illustrating an enhanced rate of electron transfer across the interface between the electrode and electrolyte solution over pristine $SrTiO_3$. Based on the above results, the schematic energy diagram of pristine $SrTiO_3$ and STO-350 is shown in Fig. 12(b). Compared with pristine $SrTiO_3$, the conduction band and valence band of STO-350 shift up, which is good for improving the reducing ability of $SrTiO_3$.

4 Conclusions

Surface reconstructed $SrTiO_3$ nanocrystals were synthesized by a thermal treatment process in presence of $NaBH_4$ and $SrTiO_3$ nanocrystals. A disordered layer was formed

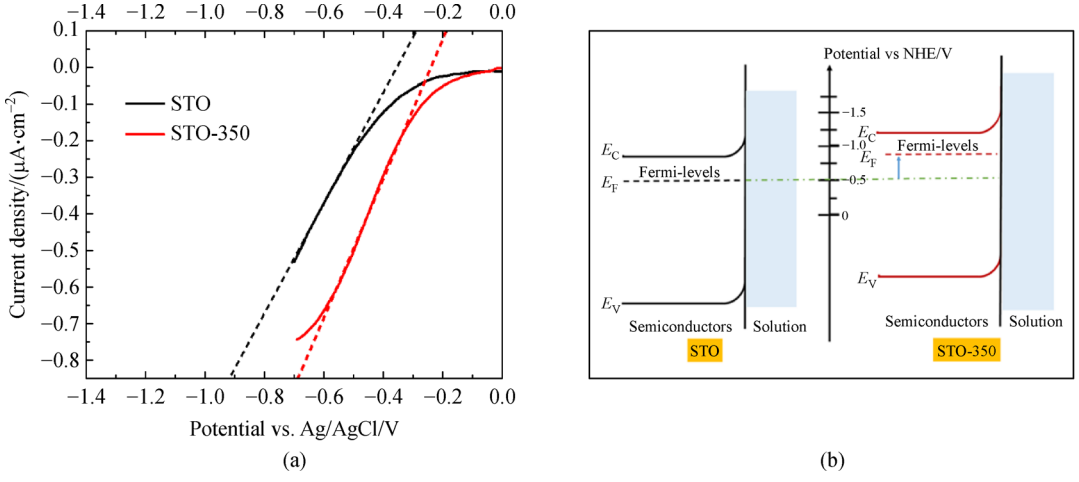

Fig. 12 LSV curves of pristine $SrTiO_3$ and STO-350.
(a) At a scan rate of 10 mV/s for hydrogen evolution reaction (HER) in 0.1 mol/L aqueous $NaSO_4$; (b) schematic energy diagram.

on the surface of the $SrTiO_3$ nanocrystals due to the introduction of oxygen vacancies. After surface reconstruction, the light absorption was extended to the infrared region, simultaneously, the charge transferability between the semiconductor and electrolyte interfaces was enhanced. Moreover, the redox potential also changed. Since there existed a synergistic effect between the three, the photocatalytic H_2 production activity of surface reconstructed $SrTiO_3$ nanocrystals was improved and the ratio of hydrogen to oxygen production was also regulated.

Acknowledgements This work was supported by the National Natural Science Foundation of China (Grant No. 21773153) and the National Key Research and Development Program of China (No. 2018YFB1502001).

Electronic Supplementary Material Supplementary material is available in the online version of this article at https://doi.org/10.1007/s11708-021-0735-2 and is accessible for authorized users.

References

1. Hong X, Tan J, Zhu H, et al. Control of spatially homogeneous distribution of heteroatoms to produce red TiO_2 photocatalyst for visible-light photocatalytic water splitting. Chemistry (Weinheim an der Bergstrasse, Germany), 2019, 25(7): 1787–1794
2. Liu J, Ke J, Li Y, et al. Co_3O_4 quantum dots/TiO_2 nanobelt hybrids for highly efficient photocatalytic overall water splitting. Applied Catalysis B: Environmental, 2018, 236: 396–403
3. Hainer A S, Hodgins J S, Sandre V, et al. Photocatalytic hydrogen generation using metal-decorated TiO_2: sacrificial donors vs. true water splitting. ACS Energy Letters, 2018, 3(3): 542–545
4. Fang W, Liu J, Yang D, et al. Effect of surface self-heterojunction existed in $Bi_xY_{1-x}VO_4$ on photocatalytic overall water splitting. ACS Sustainable Chemistry & Engineering, 2017, 5(8): 6578–6584
5. Zhou C, Shi R, Waterhouse G I, et al. Recent advances in niobium-based semiconductors for solar hydrogen production. Coordination Chemistry Reviews, 2020, 419: 213399
6. Mao L, Huang Y C, Fu Y, et al. Surface sulfurization activating hematite nanorods for efficient photoelectrochemical water splitting. Science Bulletin, 2019, 64(17): 1262–1271
7. Liu B, Jin Y, Xie G, et al. Simultaneous photocatalysis of SiC/Fe_3O_4 nanoparticles and photo-fermentation of rhodopseudomonas sp. nov. strain A7 for enhancing hydrogen production under visible light irradiation. ES Energy and Environment, 2018, 1: 56–66
8. Desai J, Baviskar P, Hui K, et al. Quadrivalently doped hematite thin films for solar water splitting. ES Energy and Environment, 2018, 2: 21–30
9. Chen X, Shi R, Chen Q, et al. Three-dimensional porous g-C_3N_4 for highly efficient photocatalytic overall water splitting. Nano Energy, 2019, 59: 644–650
10. Chiang T H, Lyu H, Hisatomi T, et al. Efficient photocatalytic water splitting using al-doped $SrTiO_3$ coloaded with molybdenum oxide and rhodium–chromium oxide. ACS Catalysis, 2018, 8(4): 2782–2788
11. Wei Y, Wang J, Yu R, et al. Constructing $SrTiO_3$-TiO_2 heterogeneous hollow multi-shelled structures for enhanced solar water splitting. Angewandte Chemie International Edition, 2019, 58(5): 1422–1426
12. Fang W, Qin Z, Liu J, et al. Photo-switchable pure water splitting under visible light over nano-Pt@ P25 by recycling scattered photons. Applied Catalysis B: Environmental, 2018, 236: 140–146
13. Guo S, Shang J, Zhao T, et al. TiO_2/cyclodextrin hybrid structure with efficient photocatalytic water splitting. ES Materials and Manufacturing, 2018, 2: 24–27
14. Macounová K M, Nebel R, Klusáčková M, et al. Selectivity control of the photo-catalytic water oxidation on $SrTiO_3$ nanocubes via surface dimensionality. ACS Applied Materials & Interfaces, 2019, 11(18): 16506–16516
15. Duong H P, Mashiyama T, Kobayashi M, et al. Z-scheme water splitting by microspherical Rh-doped $SrTiO_3$ photocatalysts prepared by a spray drying method. Applied Catalysis B: Environmental, 2019, 252: 222–229
16. Antuch M, Millet P, Iwase A, et al. Water reduction into hydrogen using Rh-doped $SrTiO_3$ photoelectrodes surface-modified by minute amounts of Pt: insights from heterogeneous kinetic analysis. Electrochimica Acta, 2019, 297: 696–704
17. Zhao Z, Goncalves R V, Barman S K, et al. Electronic structure basis for enhanced overall water splitting photocatalysis with aluminum doped $SrTiO_3$ in natural sunlight. Energy & Environmental Science, 2019, 12(4): 1385–1395
18. Ng J, Xu S, Zhang X, et al. Hybridized nanowires and cubes: a novel architecture of a heterojunctioned TiO_2/$SrTiO_3$ thin film for efficient water splitting. Advanced Functional Materials, 2010, 20(24): 4287–4294
19. Sharma D, Upadhyay S, Satsangi V R, et al. Improved photoelectrochemical water splitting performance of Cu_2O/$SrTiO_3$ heterojunction photoelectrode. Journal of Physical Chemistry C, 2014, 118 (44): 25320–25329
20. Zhong Y, Ueno K, Mori Y, et al. Plasmon-enhanced water splitting utilizing the heterojunction synergistic effect between $SrTiO_3$ and rutile-TiO_2. Chemistry Letters, 2015, 44(5): 618–620
21. Jia Y, Shen S, Wang D, et al. Composite Sr_2TiO_4/$SrTiO_3$ (La, Cr) heterojunction based photocatalyst for hydrogen production under visible light irradiation. Journal of Materials Chemistry. A, Materials for Energy and Sustainability, 2013, 1(27): 7905–7912
22. Han K, Kreuger T, Mei B, et al. Transient behavior of Ni@NiO_x functionalized $SrTiO_3$ in overall water splitting. ACS Catalysis, 2017, 7(3): 1610–1614
23. Puangpetch T, Sreethawong T, Chavadej S. Hydrogen production over metal-loaded mesoporous-assembled $SrTiO_3$ nanocrystal photocatalysts: effects of metal type and loading. International Journal of Hydrogen Energy, 2010, 35(13): 6531–6540
24. Mu L, Zhao Y, Li A, et al. Enhancing charge separation on high symmetry $SrTiO_3$ exposed with anisotropic facets for photocatalytic water splitting. Energy & Environmental Science, 2016, 9(7): 2463–2469
25. Kato H, Kobayashi M, Hara M, et al. Fabrication of $SrTiO_3$ exposing characteristic facets using molten salt flux and improvement of photocatalytic activity for water splitting. Catalysis Science & Technology, 2013, 3(7): 1733–1738

26. Wang B, Shen S, Guo L. $SrTiO_3$ single crystals enclosed with high-indexed {023} facets and {001} facets for photocatalytic hydrogen and oxygen evolution. Applied Catalysis B: Environmental, 2015, 166–167: 320–326
27. Tan H, Zhao Z, Zhu W B, et al. Oxygen vacancy enhanced photocatalytic activity of pervoskite $SrTiO_3$. ACS Applied Materials & Interfaces, 2014, 6(21): 19184–19190
28. Hu Y H. A highly efficient photocatalyst-hydrogenated black TiO_2 for the photocatalytic splitting of water. Angewandte Chemie International Edition, 2012, 51(50): 12410–12412
29. Naldoni A, Allieta M, Santangelo S, et al. Effect of nature and location of defects on bandgap narrowing in black TiO_2 nanoparticles. Journal of the American Chemical Society, 2012, 134(18): 7600–7603
30. Zhao Y, Zhao Y, Shi R, et al. Tuning oxygen vacancies in ultrathin TiO_2 nanosheets to boost photocatalytic nitrogen fixation up to 700 nm. Advanced Materials, 2019, 31(16): 1806482
31. Yu H, Shi R, Zhao Y, et al. Alkali-assisted synthesis of nitrogen deficient graphitic carbon nitride with tunable band structures for efficient visible-light-driven hydrogen evolution. Advanced Materials, 2017, 29(16): 1605148
32. Chen X, Liu L, Yu P Y, et al. Increasing solar absorption for photocatalysis with black hydrogenated titanium dioxide nanocrystals. Science, 2011, 331(6018): 746–750
33. Wang G, Ling Y, Wang H, et al. Hydrogen-treated WO_3 nanoflakes show enhanced photostability. Energy & Environmental Science, 2012, 5(3): 6180–6187
34. Li W, Liu S, Wang S, et al. The roles of reduced Ti cations and oxygen vacancies in water adsorption and dissociation on $SrTiO_3$ (110). Journal of Physical Chemistry C, 2014, 118(5): 2469–2474
35. Koocher N Z, Martirez J M P, Rappe A M. Theoretical model of oxidative adsorption of water on a highly reduced reconstructed oxide surface. Journal of Physical Chemistry Letters, 2014, 5(19): 3408–3414
36. Rabuffetti F A, Kim H S, Enterkin J A, et al. Synthesis-dependent first-order Raman scattering in $SrTiO_3$ nanocubes at room temperature. Chemistry of Materials, 2008, 20(17): 5628–5635
37. Gu L, Wei H, Peng Z, et al. Defects enhanced photocatalytic performances in $SrTiO_3$ using laser-melting treatment. Journal of Materials Research, 2017, 32(4): 748–756
38. Hashimoto S, Tanaka A. Alteration of Ti 2p XPS spectrum for titanium oxide by low-energy Ar ion bombardment. Surface and Interface Analysis, 2002, 34(1): 262–265
39. Zhang G, Jiang W, Hua S, et al. Constructing bulk defective perovskite $SrTiO_3$ nanocubes for high performance photocatalysts. Nanoscale, 2016, 8(38): 16963–16968
40. Zhang H, Cai J, Wang Y, et al. Insights into the effects of surface/bulk defects on photocatalytic hydrogen evolution over TiO_2 with exposed {001} facets. Applied Catalysis B: Environmental, 2018, 220: 126–136
41. Shetty S, Sinha S K, Ahmad R, et al. Existence of Ti^{2+} states on the surface of heavily reduced $SrTiO_3$ nanocubes. Chemistry of Materials, 2017, 29(23): 9887–9891
42. Ning X, Zhen W, Zhang X, et al. Assembly of ultra-thin NiO layer over $Zn_{1-x}Cd_xS$ for stable visible-light photocatalytic overall water splitting. ChemSusChem, 2019, 12(7): 1410–1420